Title

Refining Protein Penetration into the Lipid Bilayer Using Fluorescence Quenching and Molecular Dynamics Simulations: The Case of Diphtheria Toxin Translocation Domain

Journal

The Journal of Membrane Biology, 251(3)

ISSN

0022-2631

Authors

Kyrychenko, Alexander
Lim, Nathan M
Vasquez-Montes, Victor
et al.

Publication Date

2018-06-01

DOI

10.1007/s00232-018-0030-2

Peer reviewed

HHS Public Access

Author manuscript

J Membr Biol. Author manuscript; available in PMC 2019 June 01.

Published in final edited form as:

J Membr Biol. 2018 June ; 251(3): 379–391. doi:10.1007/s00232-018-0030-2.

Refining Protein Penetration into the Lipid Bilayer Using Fluorescence Quenching and Molecular Dynamics Simulations: The Case of Diphtheria Toxin Translocation Domain

Alexander Kyrychenko[1,2], **Nathan M. Lim**[3], **Victor Vasquez-Montes**[1], **Mykola V. Rodnin**[1], **J. Alfredo Freites**[3], **Linh P. Nguyen**[3], **Douglas J. Tobias**[3], **David L. Mobley**[3], and **Alexey S. Ladokhin**[1,*]

[1]Department of Biochemistry and Molecular Biology, Kansas University Medical Center, Kansas City, KS 66160-7421, U.S.A

[2]Institute of Chemistry and School of Chemistry, V. N. Karazin Kharkiv National University, 4 Svobody Square, Kharkiv 61022, Ukraine

[3]Department of Chemistry, University of California, Irvine, California, CA 92697-2025, U.S.A

Abstract

Dynamic disorder of the lipid bilayer presents a challenge for establishing structure-function relationships in membraneous systems. The resulting structural heterogeneity is especially evident for peripheral and spontaneously inserting membrane proteins, which are not constrained by the well-defined transmembrane topology and exert their action in the context of intimate interaction with lipids. Here we propose a concerted approach combining depth-dependent fluorescence quenching with Molecular Dynamics simulation to decipher dynamic interactions of membrane proteins with the lipid bilayers. We apply this approach to characterize membrane-mediated action of the diphtheria toxin translocation domain. First, we use a combination of the steady-state and time-resolved fluorescence spectroscopy to characterize bilayer penetration of the NBD probe selectively attached to different sites of the protein into membranes containing lipid-attached nitroxyl quenching groups. The constructed quenching profiles are analyzed with the Distribution Analysis methodology allowing for accurate determination of transverse distribution of the probe. The results obtained for 12 NBD-labeled single-Cys mutants are consistent with the so-called Open-Channel topology model. The experimentally determined quenching profiles for labeling sites corresponding to L350, N373 and P378 were used as initial constraints for positioning TH8-9 hairpin into the lipid bilayer for Molecular Dynamics simulation. Finally, we used alchemical free energy calculations to characterize protonation of E362 in soluble translocation domain and membrane-inserted conformation of its TH8-9 fragment. Our results indicate that membrane partitioning of the neutral E362 is more favorable energetically (by ~6 kcal/mol), but causes stronger perturbation of the bilayer, than the charged E362.

*To whom correspondence should be addressed: aladokhin@kumc.edu.

Keywords

diphtheria toxin; depth-dependent fluorescence quenching; distribution analysis; alchemical free energy; protonation

INTRODUCTION

Several classes of proteins insert into biological membranes in a translocon-independent manner after being refolded from the initial water-soluble structures. Examples include bacterial toxins, colicins and multiple members of the Bcl-2 family of apoptotic regulators. While in many cases the structures of soluble conformations have been determined by NMR or X-ray crystallography, the structures of the inserted forms or details of the insertion pathway, and hence many physiological aspects of their function, remain elusive (Leber et al. 2010; Moldoveanu et al. 2014; Delbridge et al. 2016). One of the main reasons for the lack in our understanding of the physiological action of these proteins is the shortage of appropriate experimental tools to study the process of their bilayer insertion. Because the refolding on the membrane interface and subsequent transbilayer insertion produces multiple intermediate states, high resolution methods are difficult to apply and structural information is teased out by various types of the fluorescence spectroscopy (Kyrychenko et al. 2017). Previously we have explored the possibility of combining fluorescence spectroscopy and Molecular Dynamics (MD) simulations to refine bilayer penetration of free and lipid-attached probes (Kyrychenko and Ladokhin 2013; Kyrychenko et al. 2014b), and simple peptides (Kyrychenko et al. 2014a). Here we extend this approach to characterize membrane interactions of the diphtheria toxin translocation (T) domain.

Refolding and membrane insertion of the T-domain occurs in response to endosomal acidification and is a key element of cellular entry of the toxin. The soluble conformation of the protein at neutral pH (Fig. 1A) consists of 9 helices of various lengths (TH1-9), eight of which completely surround the most hydrophobic one, TH8 (Choe et al. 1992; Bennett et al. 1994). Acidification initiates a series of conformational changes resulting in a poorly characterized inserted state of the protein. The central hydrophobic hairpin comprised of helices 8 and 9 is known to insert in a transmembrane orientation from numerous studies (Oh et al. 1996; Wang et al. 1997; Kachel et al. 1998; Malenbaum et al. 1998; Kyrychenko et al. 2009), however the exact position in in the bilayer has not been determined. The topologies of other hydrophobic segments TH5-7 have also been disputed (Senzel et al. 2000; Rosconi and London 2002; Ladokhin et al. 2017). To address these issues we apply a combination of steady-state and time-resolved depth-dependent fluorescence quenching (Kyrychenko and Ladokhin 2014) to determine membrane penetration of the various sites on the T-domain, selectively labeled with NBD probe (Fig. 1). The data are analyzed using Distribution Analysis methodology (Ladokhin 1997; Ladokhin 2014), previously validated using MD simulations (Kyrychenko et al. 2013 ; Kyrychenko et al. 2014b). Subsequently we use the information obtained in depth-dependent fluorescence quenching experiments to set up all-atom MD simulations of the TH8-9 helical hairpin in lipid bilayer.

pH-Triggered conformational switching in the T-domain is modulated by protonation of various histidine residues (Ladokhin 2013; Vargas-Uribe et al. 2013; Kurnikov et al. 2013; Rodnin et al. 2016), and also glutamic and aspartic acids. Recently we have demonstrated that the E362Q mutation, which removes a titratable acidic residue from the middle of TH9, shifts the pH dependence of insertion of the TH8-TH9 helices toward neutral pH (Ghatak et al. 2015). In order to quantitatively understand the role of the protonation of E362 the insertion mechanism of the T-domain, we compute the change in free energies between the charged and neutral states of E362 from simulations carried out in solution and membrane environments. Our free energy predictions indicate high favorability (~−6 kcal/mol) for neutral E362 in the membrane-protein insertion pathway, which provides a thermodynamic rationalization of previous mutagenesis results.

MATERIALS AND METHODS

Materials

1-palmitoyl-2-oleoyl-*sn*-glycero-3-phosphocholine (POPC), 1-palmitoyl-2-stearoyl-(*n*–Doxyl)-*sn*-glycero-3-phosphocholine (*n*–Doxyl–PC), and 1-palmitoyl-2-oleoyl-*sn*-glycero-3-phospho(TEMPO)choline (Tempo-PC) were obtained from Avanti Polar Lipids (Alabaster, AL). IANBD ester was obtained from Invitrogen (Carlsbad, CA). To prepare samples for depth-dependent fluorescence measurements, NBD-labeled T-domain, spin-labeled PCs and unlabeled POPC and POPG were first dissolved in chloroform solution and then dried under a high vacuum for ~12 h. The dried lipid mixtures were dissolved in 50 mM sodium phosphate buffer, pH 8, and vortexed to disperse the lipids. Large unilamellar vesicles (LUV) of 0.1 μm diameter were prepared by extrusion (Mayer et al. 1986). Lipid concentrations of stock solutions were determined according to the procedure of Bartlett (Bartlett 1959).

Preparation and Labeling of Single-Cys Mutants of T-domain

pET15b plasmid containing the diphtheria toxin T-domain gene with mutation C201S has been used as template for mutagenesis. Introduction of point Cys mutations for specific labeling with NBD derivatives was performed by site-directed mutagenesis with the QuikChange site-directed mutagenesis kit from Stratagene (Cedar Creek, TX) and verified by DNA sequencing with T7 primer. Protein expression was performed in BL21 DE3pLys Escherichia coli cells, and recombinant protein synthesis was induced by addition of 0.8 mM IPTG at OD_{600}=0.5, after which cells were grown at 25 °C overnight. Purification included affinity chromatography on Ni-NTA resin from Qiagen (Valencia, CA) and gel filtration on a Sepharose 12 1×30 cm column from GE Healthcare (Giles, U.K.) in PBS buffer containing 0.1 mM EDTA. The purity of preparations obtained was analyzed by SDS-PAGE. For determination of protein concentrations, we used a molar extinction coefficient of 17,000 M^{-1} cm^{-1} at 278 nm. Site-selective labeling with the NBD dye was performed using a standard procedure for the thiol-reactive derivatives (Rodnin et al. 2008; Kyrychenko et al. 2009).

Fluorescence Measurements

Fluorescence was measured using an SPEX Fluorolog FL3-22 steady-state fluorescence spectrometer (Jobin Yvon, Edison, NJ) equipped with double-grating excitation and emission monochromators. The measurements were made in a 2×10 mm cuvette oriented perpendicular to the excitation beam and maintained at 25 °C using a Peltier device from Quantum Northwest (Spokane, WA). For NBD measurements, the excitation wavelength was 465 nm and the slits were 5 nm. Fluorescence decays were measured with a time-resolved fluorescence spectrometer, FluoTime 200 (PicoQuant, Berlin, Germany), using a standard time-correlated single-photon counting scheme. Samples were excited at 375 nm by a subnanosecond pulsed diode laser, LDH 375 (PicoQuant, Berlin, Germany), with a repetition rate of 10 MHz. Fluorescence emission was detected at 535 nm, selected by a Sciencetech Model 9030 monochromator, using a PMA-182 photomultiplier (PicoQuant, Berlin, Germany) (Kyrychenko et al. 2009). The fluorescence intensity decay was analyzed using FluoFit iterative-fitting software based on the Marquardt algorithm (PicoQuant, Berlin, Germany).

Distribution Analysis of Depth-Dependent Quenching

Depth-dependent quenching profiles (QP's) were generated using measurements of fluorescence quenching of NBD with series of lipids labeled with spin probes at different depth, h, defined as a distance from the bilayer center. Both steady-state and time-resolved and measurements were used to determine the intensities, $F(h)$, and lifetimes, $\tau(h)$, as a function of quencher depth and the corresponding values in the absence of quenchers, F_0 and τ_0. Because of the heterogeneity of the fluorescence decay and contribution from scattering the following procedure was employed to calculate the average time of the decay (Posokhov and Ladokhin 2006): (i) time-resolved data we subjected to a standard deconvolution procedure that assumes three exponential components, with the shortest lifetime fixed at 0.1 ns; (ii) the amplitude-weighted average lifetime of the two longest components was used as the average τ. Four different QP's were generated as follows: steady-state (or total) $QP(h)=(F_0/F(h))-1$; dynamic $QP(h)=(\tau_0/\tau(h))-1$; differential $QP(h)=(F_0/F(h))-(\tau_0/\tau(h))$; and static $QP(h)=(F_0/F(h))/(\tau(h)/\tau_0)$.

Quantitative information on membrane penetration of NBD was extracted from depth-dependent quenching data using the distribution analysis (DA) methodology (Ladokhin 1997; Ladokhin 2014), which approximates the transverse quenching profile (QP) of a fluorophore with a Gaussian function, $G(h)$ (Equation 1):

$$QP(h) = G(h) + G(-h) = \frac{s}{\sigma\sqrt{2\pi}}\exp\left[-\frac{(h-h_m)^2}{2\sigma^2}\right] + \frac{s}{\sigma\sqrt{2\pi}}\exp\left[-\frac{(h+h_m)^2}{2\sigma^2}\right] \quad \text{(Eq. 1)}$$

where, h_m is the most probable depth of the probe measured from bilayer center, σ, dispersion of the transverse profile, S, overall quenching efficiency, related to lipid exposure of a probe. A symmetrical second Gaussian distribution, $G(-h)$, added to account for trans-leaflet quenching, is important for analyzing deeply penetrating fluorophores (Ladokhin 1999). Both $G(h)$ and $G(-h)$ share the three fitting parameters. The average positions of the

spin quencher, *h*, calculated from the center of the lipid bilayer have previously been determined by MD simulations of a series of spin-labeled lipids in the model membrane (Kyrychenko and Ladokhin 2013). To reduce the quenching contribution from the transverse diffusion of a probe occurring during the excited-state lifetime, we calculate the "differential" QP by subtracting the "dynamic" lifetime quenching component from the total steady-state quenching. Previously, somewhat inconsistently, we referred to it as a 'static' profile, which nevertheless increased the accuracy of depth determination in model system (Kyrychenko and Ladokhin 2014). Here, we have also calculated true static QP using the definition of Mansoor and co-workers (Mansoor et al. 2010): $QP(h)=(F_0/F(h))/(\tau(h)/\tau_0)$.

Molecular Dynamics Simulation and Free Energy Calculation Protocols

The initial protein configurations were based on the crystal structure of wild type diphtheria toxin (PDB ID 1f0l). The protein in the solution simulation system consisted of the full T domain (residues 202–378), and in the membrane system, of the TH8-TH9 hairpin (residues 319–380). TH8 is a hydrophobic helix while TH9 exhibits a significant hydrophobic moment. In the crystal structure TH8 appears fully protected by the rest of the T domain, therefore, in order to produce an initial protein configuration with favorable interactions with the membrane environment, we rotated TH9 180° about its principal axis so as to orient the polar face towards TH8 and away from the lipid bilayer hydrocarbon core. Titratable side chains were modeled consistent with neutral pH in the solution system, and with acidic pH in the membrane system. Specifically, in the solution system, all histidine residues were neutralized and acidic residues were ionized. In the membrane system, all histidine residues were charged and, except for E362, all acidic residues were neutralized. The solution simulation system was generated using VMD (Humphrey et al. 1996). The final solution system consisted of one T domain, 2768 waters and, 10 counterions for a total of 11032 atoms. The membrane system was set up by inserting the TH8-TH9 hairpin in a 1:1 POPC-POPG bilayer in excess water using the CHARMM-GUI membrane builder (Jo et al. 2009) and VMD. The final membrane system consisted of one TH8-TH9 hairpin, 250 lipids, 11724 waters, and 122 counterions for a total of 68872 atoms. Equilibration simulations were carried out at constant pressure (1 atm) and temperature (300 K) for approximately 40 ns and 113 ns for the aqueous and membrane systems, respectively.

The simulations were run with the NAMD (v2.11) software package (Phillips et al. 2005) under three-dimensional periodic boundary conditions (PBC). The protein was modeled using the CHARMM22 force field (MacKerell et al. 1998), (MacKerell et al. 2004). The CHARMM36 force field was used for lipids (Klauda et al. 2010) and the TIP3P (Jorgensen et al. 1983) model was used for water. A reversible multiple-time-step algorithm (Grubmüller et al. 1991) was used to integrate the equations of motion with a time step of 4 fs for the long-range electrostatic forces, and 2 fs for the short-range nonbonded forces and the bonded forces. The smooth particle mesh Ewald method (Essmann et al. 1995) was used to calculate electrostatic interactions. The short-range interactions were cutoff at 12 Å using a force-based switching scheme. All bond lengths involving hydrogen atoms were held fixed using the SHAKE (Ryckaert et al. 1977) and SETTLE (Miyamoto and Kollman 1992) algorithms. A Langevin dynamics scheme was used for thermostating. Nosé-Hoover-Langevin pistons were used for pressure control (Feller et al. 1995; Martyna et al. 1994).

Alchemical free energy calculations were divided into 40 equally spaced windows with production simulations running for 5 ns per stage, giving a total of 200 ns for each system. Each production run was preceded by an equilibration protocol consisting of 10000 steps of conjugate-gradient energy minimization and a 1 ns MD run. Free energies were calculated using Bennett Acceptance Ratio (Bennett 1976) as implemented by the PyMBAR program (Chodera et al. 2007), (Shirts and Chodera 2008). Corrections to the final free energies were performed using a scheme based on a continuum-electrostatics analysis, which corrects for spurious interactions encountered when simulations are carried out with periodic boundary conditions (Rocklin et al. 2013).

Trajectory analyses were performed using VMD and MDtraj (McGibbon et al. 2015). Molecular graphics were generated using VMD (Humphrey et al. 1996). Analysis of the pore resulting from the TH8-TH9 hairpin insertion in the membrane was done using dxTuber (v0.28) (Raunest and Kandt 2011). OpenDX density maps were generated using the VolMap(v1.1) plugin in VMD with the following settings: resolution: 1.0 Å atom size: 1.0 × radius, weights: mass. Density maps were combined over the final 64 ns from the membrane MD simulations. For analysis with dxTuber, we used a combination of two settings: (1) time-averaged for both the protein and solvent and (2) minimum protein density and time-averaged solvent density. Trajectory frames were aligned by the hairpin backbone using the starting frame as reference and then wrapped about the hairpin's center of mass using MDtraj (McGibbon et al. 2015).

RESULTS AND DISCUSSION

Fluorescence quenching of NBD-labeled mutants of diphtheria toxin T-domain in membranes

The membrane depth of the NBD probe attached at various positions of the T-domain was examined by depth-dependent fluorescence quenching. The steady-state and lifetime fluorescence of NBD-labeled T-domain inserted into lipid vesicles were examined in the absence and in the presence of spin-labeled lipids. To probe specific depths within a membrane, a series of six different spin probes was used, in which either Tempo or Doxyl spin quenchers are covalently attached to a phospholipid molecule. NBD-labeled T-domain and the lipid-attached spin quenchers were incorporated into POPC lipid vesicles by co-extrusion. The steady-state and time-resolved quenching were measured for the samples containing 1 μM of the labeled protein and 1 mM of LUV composed of POPC:POPG 3:1 + 30 mol % of spin-labeled lipids after 2 hours incubation in 50 mM phosphate buffer at pH 4.5. The spin moiety of Tempo or Doxyl probes is known to reside at varying depths within a membrane (Kyrychenko and Ladokhin 2013), so that they are expected to quench the NBD fluorophore of NBD-labeled T-domain to different degrees. To determine the transverse position of the NBD probe in the lipid bilayer, we constructed various depth-dependent QP's using measurements of intensity, F, and lifetime, τ, as functions of quencher depth, h (see Methods for details).

We illustrate a detailed application of quantitative analysis of depth-dependent quenching with DA methodology for the two limiting cases of shallow (P378C-NBD) and deep penetration of the probe (A282C-NBD) in Figs. 2 and 3, respectively. Panels A show the

primary experimental data for steady-state intensity (triangles) and lifetime quenching (squares). In both cases the “dynamic” quenching is much weaker than the total quenching, which is likely to be influenced by experimental difficulties of lifetime measurements in scattering samples. As a result, the “dynamic” quenching refers to all events that occur on a timescale longer than 0.1 ns (see Methods). Data in panels B and C are derived from the primary data (as defined in Methods) and represent differential QP and static QP, respectively. All datasets are fitted with Eq. 1 (solid lines) to obtain the DA parameters, including most probable depth of the fluorophore, h_m, the dispersion in transverse position, σ. The colored profiles in panels B and C represent individual Gaussian functions, G(h); while the total QP’s are a sum of G(h) and its mirror image G($-h$), accounting for the transleaflet quenching. The latter is more pronounced for the deeply penetrating probe in case of A282C-NBD (Fig. 3) and is discussed in a greater detail below.

In order to determine the robustness of the determination of the NBD penetration depth, h_m, we subjected the data to support-plane analysis procedure, described in (Montgomery and Peck 1982). Specifically, we calculated the χ^2 parameter of the goodness of the least-squares fit for a series of solutions, corresponding to values of h_m fixed at various values around the optimal (normally with a 0.2–0.5 Å step). The ratios of χ^2, calculated this way, to its minimal value, are plotted in Figs. 2D and 3D, for each of the four types of the quenching profile (color-codded curves). We used a cut-off value of 1.33 (horizontal line), to estimate the ranges of the h_m parameter that produce statistically indistinguishable fit, according to the support-plane criteria (Montgomery and Peck 1982). For a shallow penetrating fluorophore (Fig. 2D), the steady-state QP (blue), static QP (black) and differential QP (red) produce similar results, suggesting that the most probable location of the probe is between 14 and 16 Å from bilayer center. The lifetime QP is less well defined and suggests the highest dynamic component to quenching of fluorophores with the depth ranging from 16–19 Å. In contrast, the position of deeply penetrating fluorophore, A282C-NBD, is less defined (Fig. 3), primarily due to the uncertainty introduced by a cross-leaflet quenching. As the result, the distributions centered at 0 or 3 Å (individual colored profiles in Fig. 3 B–C) produce practically the same overall fit (solid lines in the same panels). Consistently, the support plane analysis indicates that the NBD’s most probable position ranges within the 4 Å range on either side of the bilayer center (Fig. 3D). Regardless of somewhat higher uncertainty, it is clear that the residue, positioned in the middle of TH5 is in the center of the bilayer, as expected in either OCS or DD models (Fig. 1).

The quenching data for all mutants are presented in Supplemental figures S1 and S2, and the summary of the application of DA to the differential QP’s are summarized in Table 1. Figures S1A–H show the DA profiles for a series of single-Cys mutants in which NBD is selectively attached along the TH9. This helix is a part of the Insertion Unit 1 (Fig. 1), known to form a transmembrane helical hairpin, with the loop translocated across the bilayer (Kyrychenko et al. 2009). As expected, the Gaussian distributions that approximate the quenching profiles (color-highlighted areas in Fig. S1) are broad due to the thermal disorder of both probe and quencher and their finite sizes. Nevertheless, the progression along the TH9 results in a monotonic decrease in average distance from bilayer center, h_m, from position 378 to 364, with subsequent increase (with a single exception) toward position 350. This pattern reflects the transmembrane orientation of the helix and the positions for the

residues could be used as both restraints for subsequent simulation (Fig. 4) and hallmarks for determining of the topology of other helices of the T-domain as well as other proteins.

To estimate the membrane topology of the Insertion Unit 2 of the T-domain (Fig. 1), we have examined DA profiles of several mutants with single Cys residues introduced into TH5 and TH6-7 fragment (Table 1, Figs. 3, S2). Attaching probes in the middle of TH5 results in deep quenching profiles, consistent with the transmembrane insertion of this helix. These data are consistent with our recent study which utilized a native fluorophore W281 as a probe and a series of lipids brominated at various positions along the acyl chain as quenchers (Ladokhin et al. 2017). In contrast, when NBD is attached at residues 305 and 312, located in TH6-7 segment, the resulting profiles are shallow at 14 Å (Fig. S2B, C). They are also very well defined, with no static quenching observed for the two deepest quenchers. We conclude that this segment does not make a transmembrane helix, but inserts close to the interface, ruling out the DD topological model (Fig. 1D). While the data are consistent with the OCS model (Fig. 1E), its functional role is not clear. Our recent study of a series of OCS-blocking mutants demonstrated that the translocation activity of the T-domain is preserved when channel activity is blocked and TH5 is not inserted into the bilayer (Ladokhin et al. 2017). It appears likely, that the OCS conformation in the wild type T-domain is formed after the translocation and plays little functional role in cellular entry of the toxin. In contrast, the insertion of the TH8-9 hairpin and its regulation by acid-induced refolding of the T-domain is a necessary prerequisite for cellular entry.

MD Simulation of the membrane-inserted TH8-9 hairpin

The positioning of TH9 along the transmembrane direction allowed us to generate a model of the membrane-inserted TH8-9 hairpin using atomistic MD simulations. We used the experimentally derived positions of L350, N373, and P378 as references in harmonic restraints applied to the geometric center of all the heavy atoms of each residue. After an ~8-ns trajectory, the three experimental restraints were satisfied with a specific tilt of TH9 and without introducing secondary structure defects (results not shown). The mean positions of the residues' geometric centers remained within the experimental DA profiles over the course of a ~113-ns unrestrained trajectory (see Fig. 4). However, all three residues exhibit a shift towards the lipid bilayer *cis* side (Fig. 4). In particular, the mean position of P378, which is on the C-terminal end of TH9 and lacks secondary structure, lies in the tail of the corresponding DA profile (approximately at 99-percentile). Yet, the overall shift of TH9 is due to a change in its orientation towards a configuration parallel to the transmembrane direction. In this new configuration, water molecules penetrate past the center of TH9, reaching E362 (Fig. 5). The deeper transmembrane location of TH9 observed in the experiments, which translates as a tilt in the restrained MD configuration, may be due to additional interactions of the TH8-9 hairpin with the rest of the T-domain, which is not present in the simulation.

Free Energies indicate high favorability for neutralized E362

In our free energy calculations, we alchemically transform the glutamic acid residue at position 362 from its charged to neutral state by effectively creating or annihilating a proton on the terminal oxygen atom, denoted as OE2 from the CHARMM 22 topology. Our initial

state is with the charged residue in the aqueous solution and our end state is that of the neutral residue within the membrane environment. To determine the T-domain insertion free energies, we apply the thermodynamic cycle illustrated in Figure 6 and obtain Equation 2. Here, we define our four terms: $\Delta G_{aq}^{E362}(Chg \rightarrow Ntrl)\Delta G_{aq}^{E362}(Chg \rightarrow Net)$ represents the change in free energy of altering the charged residue E362 to neutral in the aqueous environment while $\Delta G_{mem}^{E362}(Chg \rightarrow Ntrl)$ represents the same charge change but in the membrane environment. The membrane-protein insertion free energy is represented by the terms $\Delta G_{aq\rightarrow mem}^{E362}(Ntrl)\Delta G_{aq\rightarrow mem}^{E362}(Net)$ and $\Delta G_{aq\rightarrow mem}^{E362}(Chg)$, whereby residue E362 is either in the neutral *(Ntrl)* state or the charged *(Chg)* state. From rearranging, we show that the free energy difference from insertion of the neutral versus charged system is equivalent to the free energy change resulting from the perturbation of the residue in the aqueous versus membrane environment (Equation 3). Thus, the total membrane-protein insertion free energy can be obtained from either pair of terms. Since we cannot conduct MD simulations corresponding to the vertical legs from Figure 6 to obtain the free energies denoted in Equation 4, we instead obtain the insertion free energy from the equivalent terms in the cycle. Thus, from Equation 5, the total insertion free energy can obtained from the MD free energy simulations where we perturb the residue in both the aqueous and membrane environments.

$$0 = \Delta G_{aq}^{E362}(Chg \rightarrow Ntrl) + \Delta G_{aq\rightarrow mem}^{E362}(Ntrl) - \Delta G_{mem}^{E362}(Chg \rightarrow Ntrl) - \Delta G_{aq\rightarrow mem}^{E362}(Chg)$$

(Eq. 2)

$$\Delta G_{aq\rightarrow mem}^{E362}(Ntrl) - \Delta G_{aq\rightarrow mem}^{E362}(Chg) = \Delta G_{mem}^{E362}(Chg \rightarrow Ntrl) - \Delta G_{aq}^{E362}(Chg \rightarrow Ntrl) \quad \text{(Eq. 3)}$$

$$\Delta\Delta G_{aq\rightarrow mem}^{E362}(Ntrl) = \Delta G_{aq\rightarrow mem}^{E362}(Ntrl) - \Delta G_{aq\rightarrow mem}^{E362}(Chg) \quad \text{(Eq. 4)}$$

$$\Delta\Delta G_{aq\rightarrow mem}^{E362}(Ntrl) = \Delta G_{mem}^{E362}(Chg \rightarrow Ntrl) - \Delta G_{aq}^{E362}(Chg \rightarrow Ntrl) \quad \text{(Eq. 5)}$$

From our calculations (Table 2), the free energy change obtained from alchemically creating a proton to neutralize the charged glutamic residue was +84.4 kcal/mol in the membrane and +86.0 kcal/mol in the aqueous environment, yielding a final insertion free energy of −1.6 kcal/mol. As our simulated system was neutralized with counterions when E362 was charged, the alchemical modification being made here results in the overall system becoming non-neutral. This gives rise to significant artifacts arising from self-interactions through neighboring periodic copies, which can dramatically impact our computed free

energy differences. A correction scheme for the self-interactions has been previously described in a similar membrane-insertion free energy study, conducted on outer membrane phospholipase A (OmpLA) (Gumbart and Roux 2012). In this scheme described by Gumbart and Roux, they intentionally neglect the self-interaction from the charged residue and its periodic replicas-on account of the term being negligible due to the pore waters shielding the charge. As our simulations of T-domain involve a much narrower pore and thus were uncertain if water would effectively shield the charge, we employed a more thorough correction scheme based on a continuum-electrostatics analysis (Rocklin et al. 2013). After applying the analytical continuum-electrostatics scheme described by Rocklin et. al, our corrected insertion free energy was −6.2 ± 0.4 kcal/mol, which suggests high favorability for the neutralized residue in the membrane insertion pathway..

Neutralized E362 produces a larger membrane perturbation

We have examined the effect of protonation state of E362 on the local perturbation of the bilayer. Through time-averaged density maps of the protein and solvent over the course of the MD simulations, we show that the pore created by T-domain TH8-9 hairpin and the inner tunnel-like cavity are larger when residue E362 is neutralized. Thus, we provide supporting evidence on the importance of residue E362 and its pH-dependent conformational switching for perturbing the membrane to allow for insertion.

From our MD simulations, we found that the exposure of the charge on residue E362 within the membrane environment results in the two helices moving closer together to effectively shield the unfavorable charge in the center of the surrounding non-polar membrane environment. When residue E362 is charged, the two helices are pulled together by formation of a hydrogen bond network primarily involving residues surrounding E362. From Figure 7, we show residues S336 and S337 on the TH8 helix are oriented inward in order to more closely interact with residues N366, S363, and charged E362 on the opposing TH9 helix. From calculating the percent occupancy of hydrogen bond contacts between S336 and S363 – the two closest residues on opposing helices – we find that when residue E362 is neutral, hydrogen bonding occurs in roughly 57% of trajectory frames, but when E362 is charged the hydrogen bonding occurs in approximately 88% of the trajectory frames. Our analysis of the MD trajectories indicates that when E362 is charged, the two helices are drawn closer together, thereby decreasing the overall perturbation to the membrane. This finding suggests favorability for neutralized over charged E362 during the membrane insertion mechanism as formation of a larger pore could better facilitate delivery of the catalytic domain across the membrane.

In order to approximate the pore size from T-domain insertion, we use dxTuber to calculate the cross-sectional area along the membrane normal over the course of the MD trajectories. By using the average protein and average solvent densities, we generate a time-averaged map of solvent accessibility around the protein (Figure 7), colored according to the averaged density (red=high density; blue=low). From our analysis (Table 3), we find that the average cross-sectional area when residue E362 is neutral is 750 $Å^2$ and when charged is 740 $Å^2$. Next, by using the minimum protein densities with averaged solvent densities, we filter out regions of high protein flexibility. This yields a map of the areas with maximum solvent

accessibility, which appears to map the solvent accessibility of the pore interior (Figure 8). The average cross-sectional area through the inner cavity when residue E362 is neutral is 318 $Å^2$ and when charged is 217 $Å^2$. Both the average and minimum protein profiles indicate the pore formed in the membrane by T-domain insertion is larger when residue E362 is neutralized. This analysis provides further evidence that membrane perturbation starts with the initial insertion of TH8-9 domain and that E362 may play multiple roles in modulating the insertion mechanism of the T-domain.

SUMMARY

In this study we present a novel approach for characterizing structural aspects of the membrane penetration of proteins *via* a combination of fluorescence spectroscopy and MD simulations. Using site-selective labeling combined with steady-state and time-resolved depth-dependent fluorescence quenching, we have generated depth-dependent quenching profiles for the 12 NBD-labeling positions in membrane-inserted diphtheria toxin translocation domain (Fig. 1). The transverse positions of the labeled residues within the bilayer were estimated using Distribution Analysis approach (Figs. 2, 3, S1, S2 Table 1) and were found them consistent with the Open-Channel State topological model (Fig. 1). Quenching-based estimates of the most probable bilayer depth of L350, N373 and P378 residues were used as restraints for setting up a MD simulation of the TH8-9 hydrophobic hairpin in a lipid bilayer (Figs. 1B, 4, 5). The alchemical free energy calculations for the critical titratable residue E362 (Fig. 6, Table 2) revealed a 6 kcal/mol difference favoring the membrane partitioning of the protonated form vs. the ionized form, thus providing important thermodynamic insights into pH-triggered conformational switching during bilayer insertion. Solvent accessibility calculations revealed that neutral form of E362 perturbs the integrity of the lipid bilayer (Figs. 8, 9), providing atomistic insights into pH-dependent interactions of the T-domain with the lipid bilayer. The proposed methodology, which combines fluorescence quenching and MD simulations, can be used for extracting valuable structural and thermodynamic details relevant to physiological action of a variety of bilayer-inserted proteins.

Supplementary Material

Refer to Web version on PubMed Central for supplementary material.

Acknowledgments

This research was supported in part by National Institutes of Health Grant P30-GM110761. A.K. also acknowledges support of Grant 0116U000835 of Ministry of Education and Science of Ukraine.

ABBREVIATIONS

Tempo-PC	1-palmitoyl-2-oleoyl-*sn*-glycero-3-phospho(TEMPO)choline
***n*-Doxyl-PC**	1-palmitoyl-2-stearoyl-(*n*-Doxyl)-*sn*-glycero-3-phosphocholine

POPC	1-palmitoyl-2-oleoyl-*sn*-glycero-3-phosphocholine
POPG	1-palmitoyl-2-oleoyl-*sn*-glycero-3-phosphoglycerol
LUV	large unillamelar vesicles
MD	molecular dynamics
DA	Distribution Analysis
QP	Quenching Profile

References

Bartlett GR. Phosphorus assay in column chromatography. JBiolChem. 1959; 234:466–468.

Bennett CH. Efficient estimation of free energy differences from Monte Carlo data. Journal of Computational Physics. 1976; 22:245–268.

Bennett MJ, Choe S, Eisenberg D. Refined structure of dimeric diphtheria toxin at 2.0 Å resolution. Protein Sci. 1994; 3:1444–1463. [PubMed: 7833807]

Chodera JD, Swope WC, Pitera JW, Seok C, Dill KA. Use of the Weighted Histogram Analysis Method for the Analysis of Simulated and Parallel Tempering Simulations. J Chem Theory Comput. 2007; 3:26–41. [PubMed: 26627148]

Choe S, Bennett MJ, Fujii G, Curmi PMG, Kantardjieff KA, Collier RJ, Eisenberg D. The Crystal Structure of Diphtheria Toxin. Nature. 1992; 357:216–222. [PubMed: 1589020]

Delbridge AR, Grabow S, Strasser A, Vaux DL. Thirty years of BCL-2: translating cell death discoveries into novel cancer therapies. Nature reviews Cancer. 2016; 16:99–109. [PubMed: 26822577]

Essmann U, Perera L, Berkowitz ML, Darden T, Lee H, Pedersen LG. A smooth particle mesh Ewald method. JChemPhys. 1995; 103:8577–8593.

Feller SE, Zhang Y, Pastor RW, Brooks BR. Constant pressure molecular dynamics simulation: The Langevin piston method. JChemPhys. 1995; 103:4613–4621.

Ghatak C, Rodnin MV, Vargas-Uribe M, McCluskey AJ, Flores-Canales JC, Kurnikova M, Ladokhin AS. Role of Acidic Residues in Helices TH8–TH9 in Membrane Interactions of the Diphtheria Toxin T Domain. Toxins. 2015; 7:1303–1323. [PubMed: 25875295]

Grubmüller H, Heller H, Windemuth A, Schulten K. Generalized Verlet algorithm for efficient molecular dynamics simulations with long-range interactions. Molecular Simulation. 1991; 6:121–142.

Gumbart J, Roux B. Determination of Membrane-Insertion Free Energies by Molecular Dynamics Simulations. Biophysical journal. 2012; 102:795–801. [PubMed: 22385850]

Humphrey W, Dalke A, Schulten K. VMD: visual molecular dynamics. Journal of molecular graphics. 1996; 14:33–38. [PubMed: 8744570]

Jo S, Lim JB, Klauda JB, Im W. CHARMM-GUI Membrane Builder for Mixed Bilayers and Its Application to Yeast Membranes. Biophysical journal. 2009; 97:50–58. [PubMed: 19580743]

Jorgensen WL, Chandrasekhar J, Madura JD, Impey RW, Klein ML. Comparison of simple potential functions for simulating liquid water. JChemPhys. 1983; 79:926–935.

Kachel K, Ren JH, Collier RJ, London E. Identifying transmembrane states and defining the membrane insertion boundaries of hydrophobic helices in membrane-inserted diphtheria toxin T domain. JBiolChem. 1998; 273:22950–22956.

Klauda JB, Venable RM, Freites JA, O'Connor JW, Tobias DJ, Mondragon-Ramirez C, Vorobyov I, MacKerell AD Jr, Pastor RW. Update of the CHARMM all-atom additive force field for lipids: validation on six lipid types. The journal of physical chemistry B. 2010; 114:7830–7843. [PubMed: 20496934]

Kurnikov IV, Kyrychenko A, Flores-Canales JC, Rodnin MV, Simakov N, Vargas-Uribe M, Posokhov YO, Kurnikova M, Ladokhin AS. pH-Triggered Conformational Switching of the Diphtheria Toxin

T-Domain: The Roles of N-Terminal Histidines. J Mol Biol. 2013; 425:2752–2764. [PubMed: 23648837]

Kyrychenko A, Freites JA, He J, Tobias DJ, Wimley WC, Ladokhin AS. Structural plasticity in the topology of the membrane-interacting domain of HIV-1 gp41. Biophysical journal. 2014a; 106:610–620. [PubMed: 24507601]

Kyrychenko A, Ladokhin AS. Molecular Dynamics Simulations of Depth Distribution of Spin-Labeled Phospholipids within Lipid Bilayer. The journal of physical chemistry B. 2013; 117:5875–5885. [PubMed: 23614631]

Kyrychenko A, Ladokhin AS. Refining membrane penetration by a combination of steady-state and time-resolved depth-dependent fluorescence quenching. Analytical biochemistry. 2014; 446:19–21. [PubMed: 24141077]

Kyrychenko A, Posokhov YO, Rodnin MV, Ladokhin AS. Kinetic intermediate reveals staggered pH-dependent transitions along the membrane insertion pathway of the diphtheria toxin T-domain. Biochemistry. 2009; 48:7584–7594. [PubMed: 19588969]

Kyrychenko, A., Posokhov, YO., Vargas-Uribe, M., Ghatak, C., Rodnin, MV., Ladokhin, AS. Fluorescence Applications for Structural and Thermodynamic Studies of Membrane Protein Insertion. In: Geddes, CD., editor. Reviews in Fluorescence. Vol. 2016. Springer; 2017. p. 243-274.

Kyrychenko A, Rodnin MV, Ladokhin AS. Calibration of Distribution Analysis of the Depth of Membrane Penetration Using Simulations and Depth-Dependent Fluorescence Quenching. The Journal of membrane biology. 2014b

Kyrychenko A, Tobias DJ, Ladokhin AS. Validation of Depth-Dependent Fluorescence Quenching in Membranes by Molecular Dynamics Simulation of Tryptophan Octyl Ester in POPC Bilayer. The journal of physical chemistry B. 2013; 117:4770–4778. [PubMed: 23528135]

Ladokhin AS. Distribution analysis of depth-dependent fluorescence quenching in membranes: A practical guide. Methods Enzymol. 1997; 278:462–473. [PubMed: 9170327]

Ladokhin AS. Analysis of protein and peptide penetration into membranes by depth-dependent fluorescence quenching: Theoretical considerations. Biophys J. 1999; 76:946–955. [PubMed: 9929496]

Ladokhin AS. pH-triggered conformational switching along the membrane insertion pathway of the diphtheria toxin T-domain. Toxins. 2013; 5:1362–1380. [PubMed: 23925141]

Ladokhin AS. Measuring membrane penetration with depth-dependent fluorescence quenching: distribution analysis is coming of age. Biochimica et biophysica acta. 2014; 1838:2289–2295. [PubMed: 24593994]

Ladokhin SA, Vargas-Uribe M, Rodnin VM, Ghatak C, Sharma O. Cellular Entry of the Diphtheria Toxin Does Not Require the Formation of the Open-Channel State by Its Translocation Domain. Toxins. 2017; 9

Leber B, Lin J, Andrews DW. Still embedded together binding to membranes regulates Bcl-2 protein interactions. Oncogene. 2010; 29:5221–5230. [PubMed: 20639903]

MacKerell AD, Feig M, Brooks CL. Extending the treatment of backbone energetics in protein force fields: Limitations of gas-phase quantum mechanics in reproducing protein conformational distributions in molecular dynamics simulations. Journal of computational chemistry. 2004; 25:1400–1415. [PubMed: 15185334]

MacKerell AD Jr, Bashford D, Bellott M, Dunbrack RL Jr, Evanseck JD, Field MJ, Fischer S, Gao J, Guo H, Ha S, Joseph-McCarthy D, Kuchnir L, Kuczera K, Lau FTK, Mattos C, Michnick S, Ngo T, Nguyen DT, Prodhom B, Reiher WE III, Roux B, Schlenkrich M, Smith JC, Stote R, Straub J, Watanabe M, Wiórkiewicz-Kuczera J, Yin D, Karplus M. All-atom empirical potential for molecular modeling and dynamics studies of proteins. JPhysChemB. 1998; 102:3586–3616.

Malenbaum SE, Collier RJ, London E. Membrane topography of the T domain of diphtheria toxin probed with single tryptophan mutants. Biochemistry. 1998; 37:17915–17922. [PubMed: 9922159]

Mansoor SE, DeWitt MA, Farrens DL. Distance Mapping in Proteins Using Fluorescence Spectroscopy: The Tryptophan-Induced Quenching (TrIQ) Method. Biochemistry. 2010; 49:9722–9731. [PubMed: 20886836]

Martyna GJ, Tobias DJ, Klein ML. Constant-pressure molecular-dynamics algorithms. Journal of Chemical Physics. 1994; 101:4177–4189.

Mayer LD, Hope MJ, Cullis PR. Vesicles of variable sizes produced by a rapid extrusion procedure. BiochimBiophysActa. 1986; 858:161–168.

McGibbon Robert T, Beauchamp Kyle A, Harrigan Matthew P, Klein C, Swails Jason M, Hernández Carlos X, Schwantes Christian R, Wang L-P, Lane Thomas J, Pande Vijay S. MDTraj: A Modern Open Library for the Analysis of Molecular Dynamics Trajectories. Biophysical journal. 2015; 109:1528–1532. [PubMed: 26488642]

Miyamoto S, Kollman PA. Settle: An analytical version of the SHAKE and RATTLE algorithm for rigid water models. Journal of computational chemistry. 1992; 13:952–962.

Moldoveanu T, Follis AV, Kriwacki RW, Green DR. Many players in BCL-2 family affairs. Trends in biochemical sciences. 2014; 39:101–111. [PubMed: 24503222]

Montgomery, DC., Peck, EA. Introduction to linear regression analysis. Wiley; New York: 1982.

Oh KJ, Zhan H, Cui C, Hideg K, Collier RJ, Hubbell WL. Organization of diphtheria toxin T domain in bilayers: A site-directed spin labeling study. Science. 1996; 273:810–812. [PubMed: 8670424]

Phillips JC, Braun R, Wang W, Gumbart J, Tajkhorshid E, Villa E, Chipot C, Skeel RD, Kalé L, Schulten K. Scalable molecular dynamics with NAMD. Journal of computational chemistry. 2005; 26:1781–1802. [PubMed: 16222654]

Posokhov YO, Ladokhin AS. Lifetime fluorescence method for determining membrane topology of proteins. Analytical biochemistry. 2006; 348:87–93. [PubMed: 16298322]

Raunest M, Kandt C. dxTuber: Detecting protein cavities, tunnels and clefts based on protein and solvent dynamics. Journal of Molecular Graphics and Modelling. 2011; 29:895–905. [PubMed: 21420887]

Rocklin GJ, Mobley DL, Dill KA, Hunenberger PH. Calculating the binding free energies of charged species based on explicit-solvent simulations employing lattice-sum methods: an accurate correction scheme for electrostatic finite-size effects. The Journal of chemical physics. 2013; 139:184103. [PubMed: 24320250]

Rodnin MV, Li J, Gross ML, Ladokhin AS. The pH-Dependent Trigger in Diphtheria Toxin T Domain Comes with a Safety Latch. Biophysical journal. 2016; 111:1946–1953. [PubMed: 27806276]

Rodnin MV, Posokhov YO, Contino-Pepin C, Brettmann J, Kyrychenko A, Palchevskyy SS, Pucci B, Ladokhin AS. Interactions of fluorinated surfactants with diphtheria toxin T-domain: testing new media for studies of membrane proteins. Biophysical journal. 2008; 94:4348–4357. [PubMed: 18310255]

Rosconi MP, London E. Topography of helices 5–7 in membrane-inserted diphtheria toxin T domain: identification and insertion boundaries of two hydrophobic sequences that do not form a stable transmembrane hairpin. The Journal of biological chemistry. 2002; 277:16517–16527. [PubMed: 11859081]

Ryckaert J-P, Ciccotti G, Berendsen HJC. Numerical integration of the Cartesian equations of motion of a system with constraints: Molecular dynamics of *n*-alkanes. Journal of Computational Physics. 1977; 23:327–341.

Senzel L, Gordon M, Blaustein RO, Oh KJ, Collier RJ, Finkelstein A. Topography of diphtheria toxin's T domain in the open channel state. JGenPhysiol. 2000; 115:421–434.

Shirts MR, Chodera JD. Statistically optimal analysis of samples from multiple equilibrium states. The Journal of chemical physics. 2008; 129:124105. [PubMed: 19045004]

Vargas-Uribe M, Rodnin MV, Kienker P, Finkelstein A, Ladokhin AS. Crucial Role of H322 in Folding of the Diphtheria Toxin T-Domain into the Open-Channel State. Biochemistry. 2013; 52:3457–3463. [PubMed: 23621842]

Wang Y, Malenbaum SE, Kachel K, Zhan HJ, Collier RJ, London E. Identification of shallow and deep membrane-penetrating forms of diphtheria toxin T domain that are regulated by protein concentration and bilayer width. JBiolChem. 1997; 272:25091–25098.

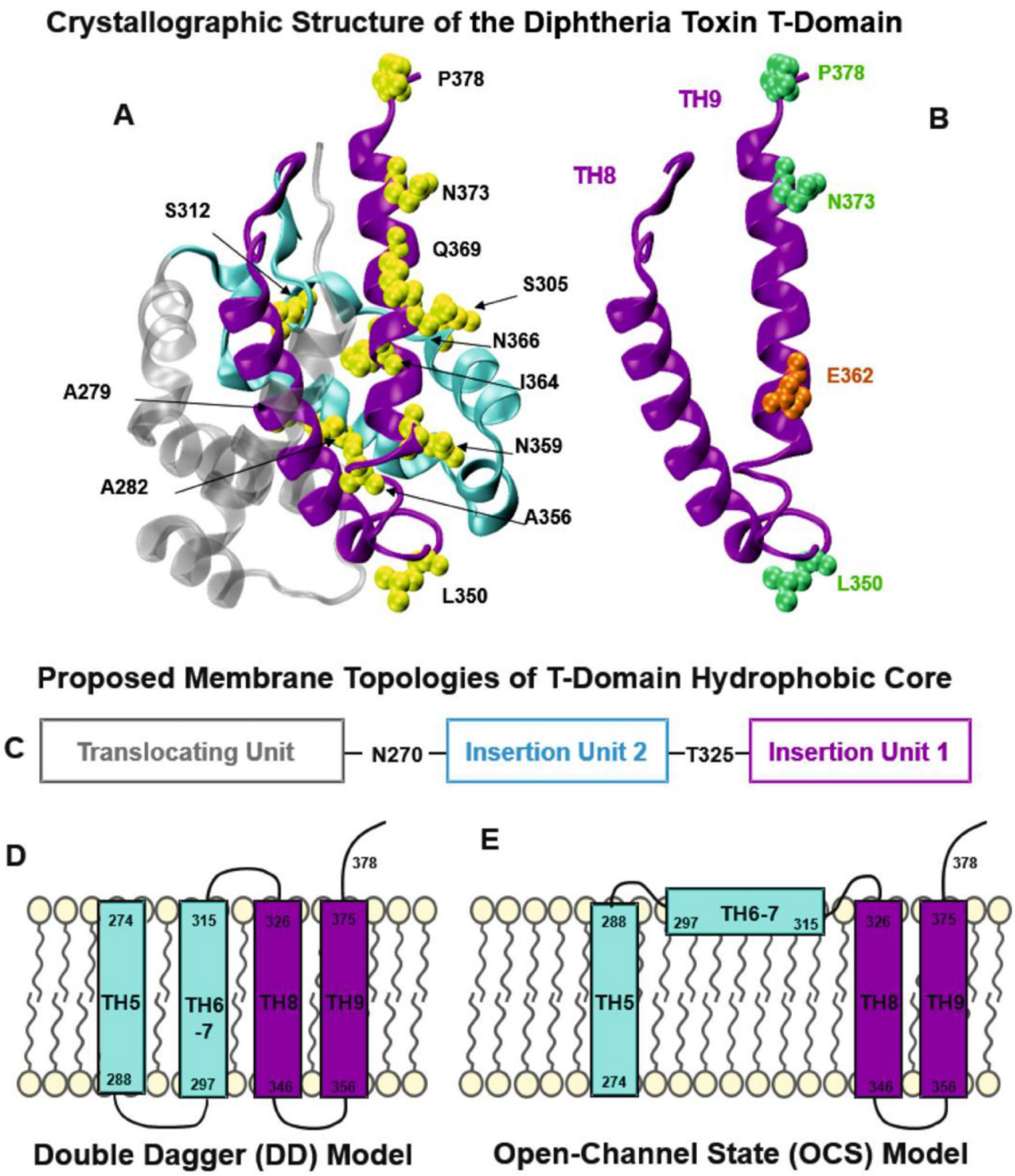

Figure 1. Solution Structure and Membrane Topology of the T-Domain

(A) Ribbon diagram representation of the structure of the T-domain from crystallographic study of diphtheria toxin translocation domain from (Bennett et al. 1994) with helices TH8 and TH9 highlighted in magenta (also shown separately in panel B), TH5 through TH7 in cyan, and TH1 throughTH1 as grey ribbons (the color scheme corresponds to suggested partitioning of the sequence into three fragments, illustrated in C). Residues mutated for NBD-labeling are shown as CPK representations in yellow. (B) The crystallographic structure of the TH8-9 helical hairpin used in MD simulation in lipid bilayer with the three residues used for MD simulation restrain positions are shown in green. Residue E362 used

in free energy calculations of protonation is shown in orange. (C–E) Proposed membrane topologies of the T-domain. Two alternative Double Dagger (DD) and Open-Channel State (OCS) topological schemes, shown in (D) and (E), respectively, are redrawn from (Senzel et al. 2000). Depth-dependent fluorescence quenching data presented here exclude the DD topology.

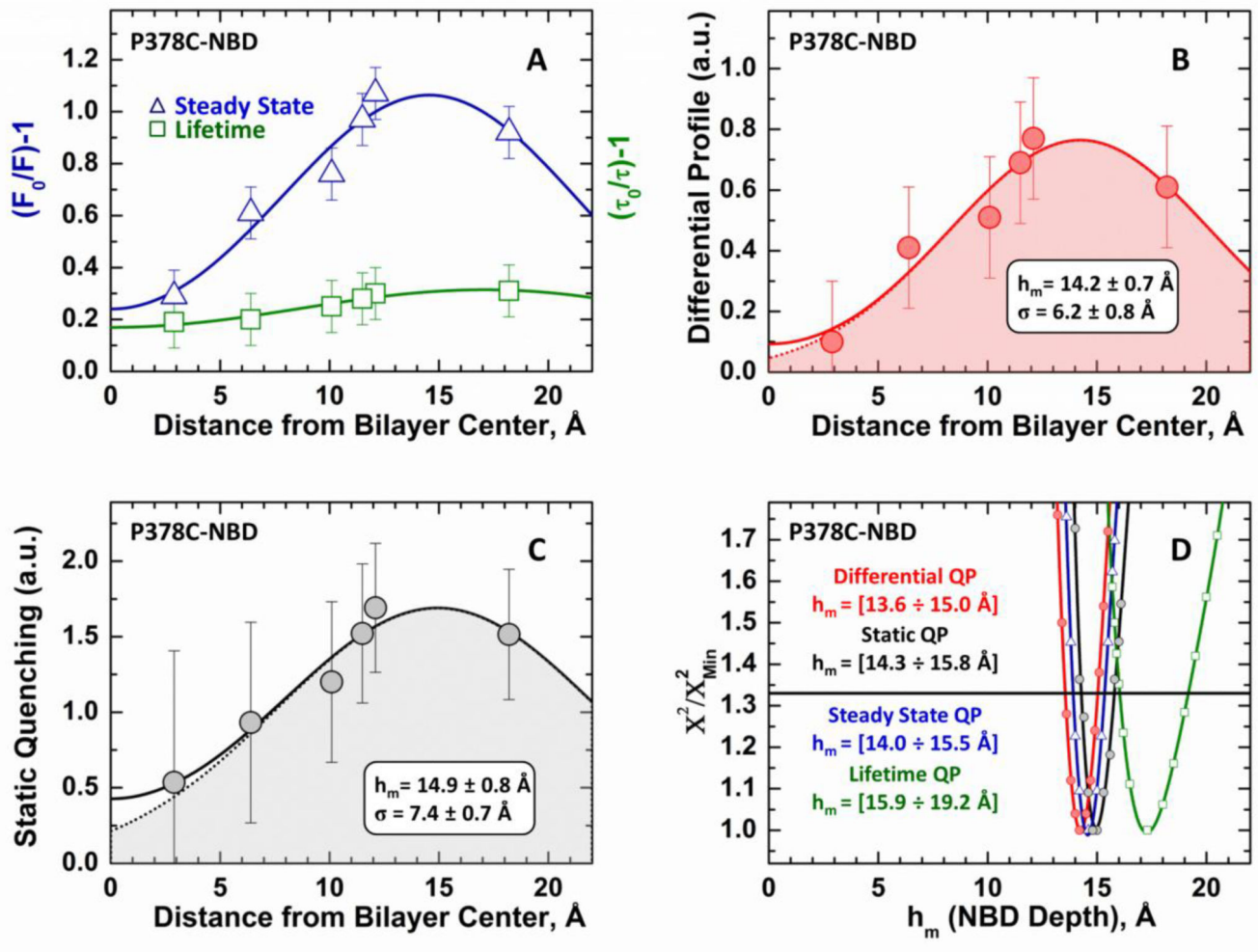

Figure 2. Application of Distribution Analysis (DA) to depth-dependent fluorescence quenching of shallow penetrating probe in P378C-NBD mutant

(A) Fluorescence steady-state (triangles) and time-resolved (squares) quenching profiles plotted against the depth of the following quenchers (from right to left): Tempo–PC and *n*-Doxyl–PCs with n = 5, 7, 10, 12, and 14. (B) Differential QP, calculated from the data in panel A as $(F_0/F(h))-(\tau_0/\tau(h))$. (C) static QP$(h)=(F_0/F(h))/(\tau(h)/\tau_0)$. Solid lines represent the fit of the corresponding datasets using DA (Eq. 1). The shaded areas represent a Gaussian function for the single leaflet quenching profiles. The sum of the shaded area, G(*h*), and its mirror image, G(−*h*), represents the total fitting function of DA, with the total of three fitting parameters: h_m, σ and *S* (indicated on panels B and C and in Table 1). (D) Support-plane analysis of the robustness of the determination of the parameter for the most probable depth of the NBD dye (see text for details).

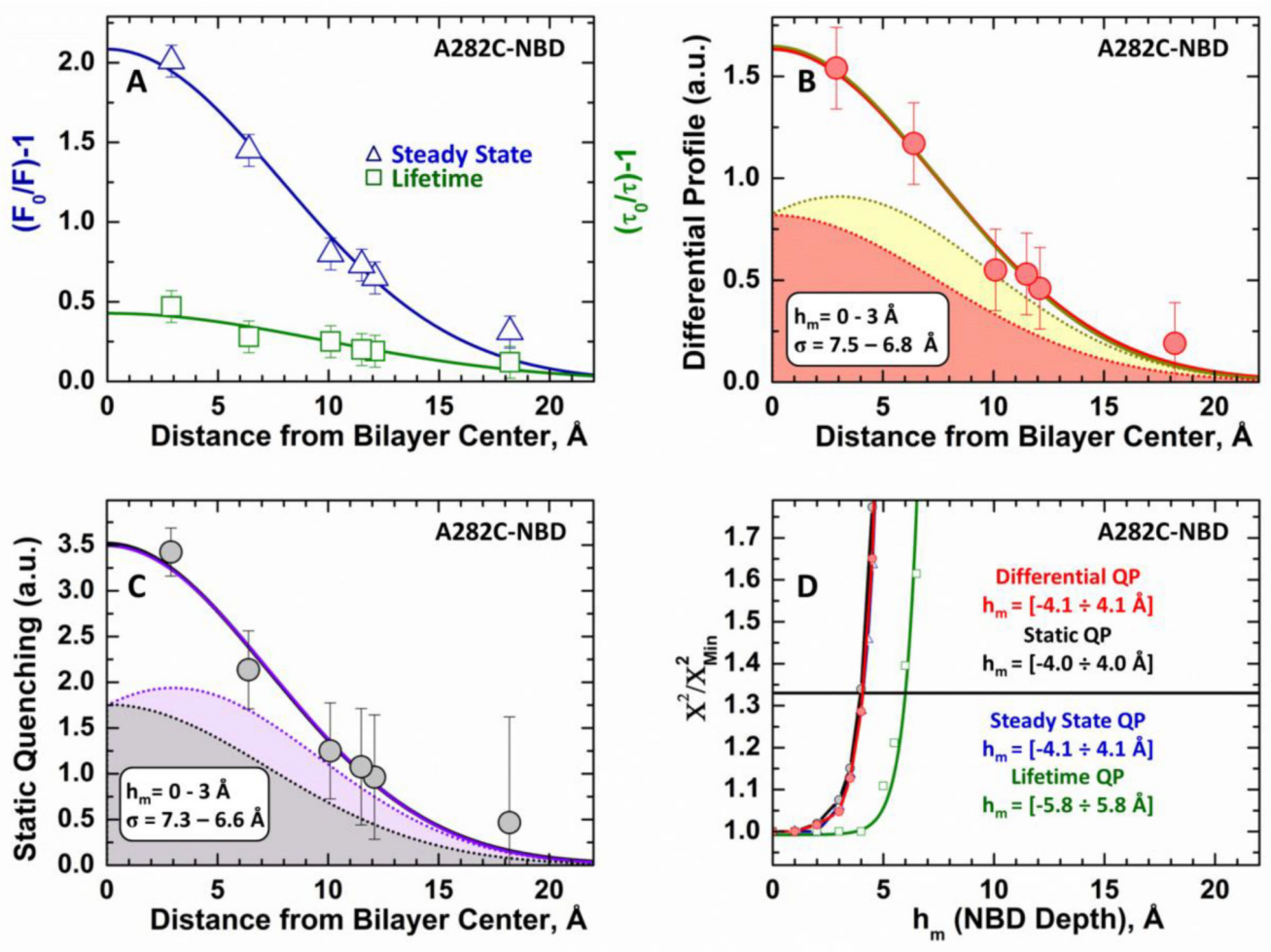

Figure 3. Application of DA to depth-dependent fluorescence quenching of deep penetrating probe in A282C-NBD mutant

The steady-state (panel A, triangles) and time-resolved data (panel A, squares), as well as differential (panel B) and static (panel C) quenching profiles were obtained as described in Fig. 2. Solid shapes represent two examples of individual solutions for a single-leaflet quenching profile (G(*h*) in Eq. 1) with h_m=0 Å (red in B, grey in C) and h_m=3 Å (yellow in B, purple in C). Both solutions produce essentially overlapping two-leaflet quenching profiles (correspondingly colored solid lines that go through the data in panels B and C), defined in Eq. 1 as a sum of G(*h*) and its mirror-image, G(−*h*). (D) Support-plane analysis of the robustness of the determination of the parameter for the most probable depth of the NBD dye (see text for details).

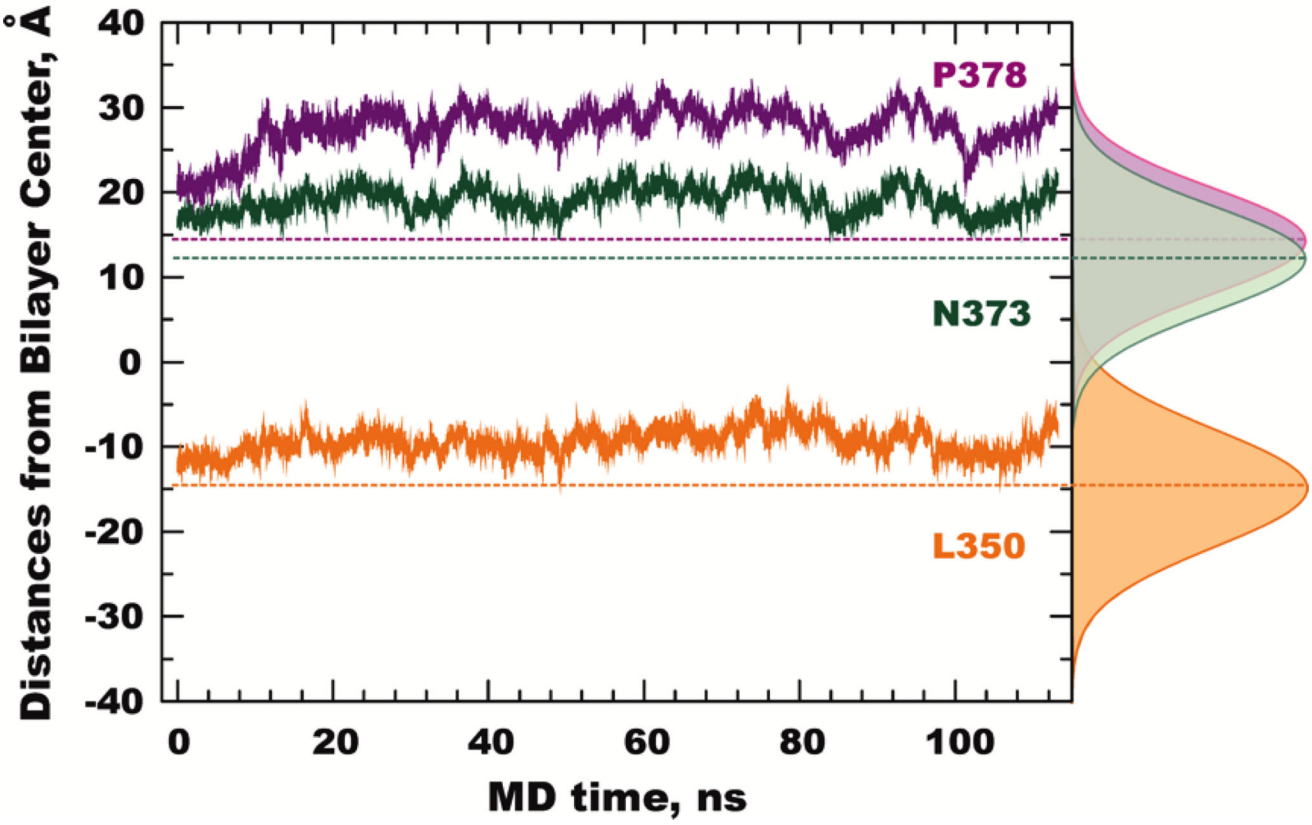

Figure 4. MD simulations of immersion depths of T-domain residues

Time-traces of the bilayer immersion depths of residues L350, N373 and P378 derived from an unrestrained MD simulation. The corresponding depth distributions estimated by DA are shown as color-coded shaded profiles (the center of the DA profile h_m is plotted with a dotted line).

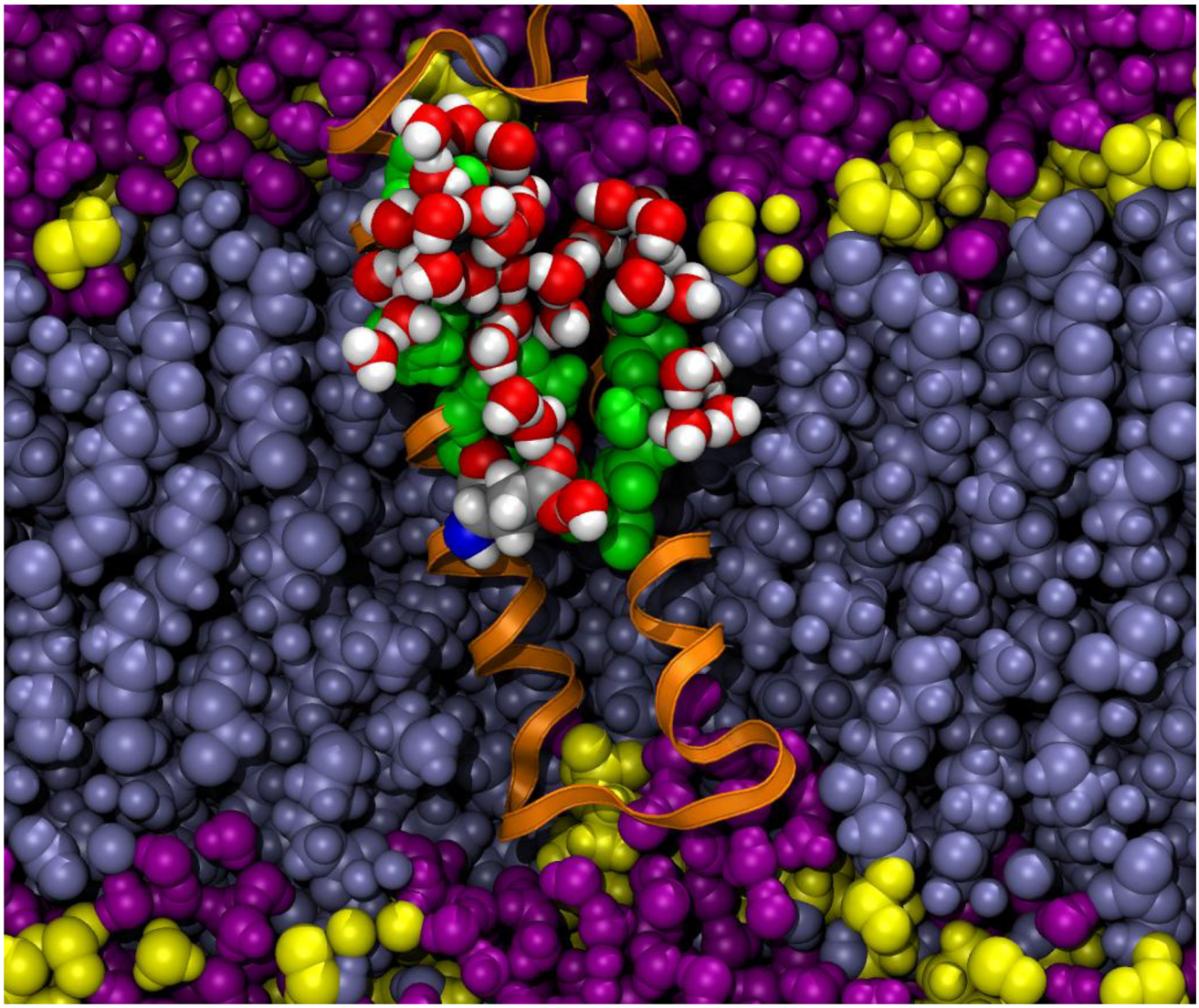

Figure 5.

Membrane-inserted model of the TH8-9 hairpin in a cut-away view of the lipid bilayer. Through solvation of polar side chains (residues 332, 336, 337, 363, 369, and 373; shown in green), water molecules penetrate deeply into the membrane in order to solvate E362 (colored by atom type: carbon, silver; nitrogen, blue; oxygen, red; hydrogen, white). Waters within the solvation shell of these residues are colored by atom type. Other water molecules are colored purple. The helical hairpin is shown in ribbon representation (in orange). The lipid bilayer headgroups are colored yellow, and lipid acyl chains are colored ice blue.

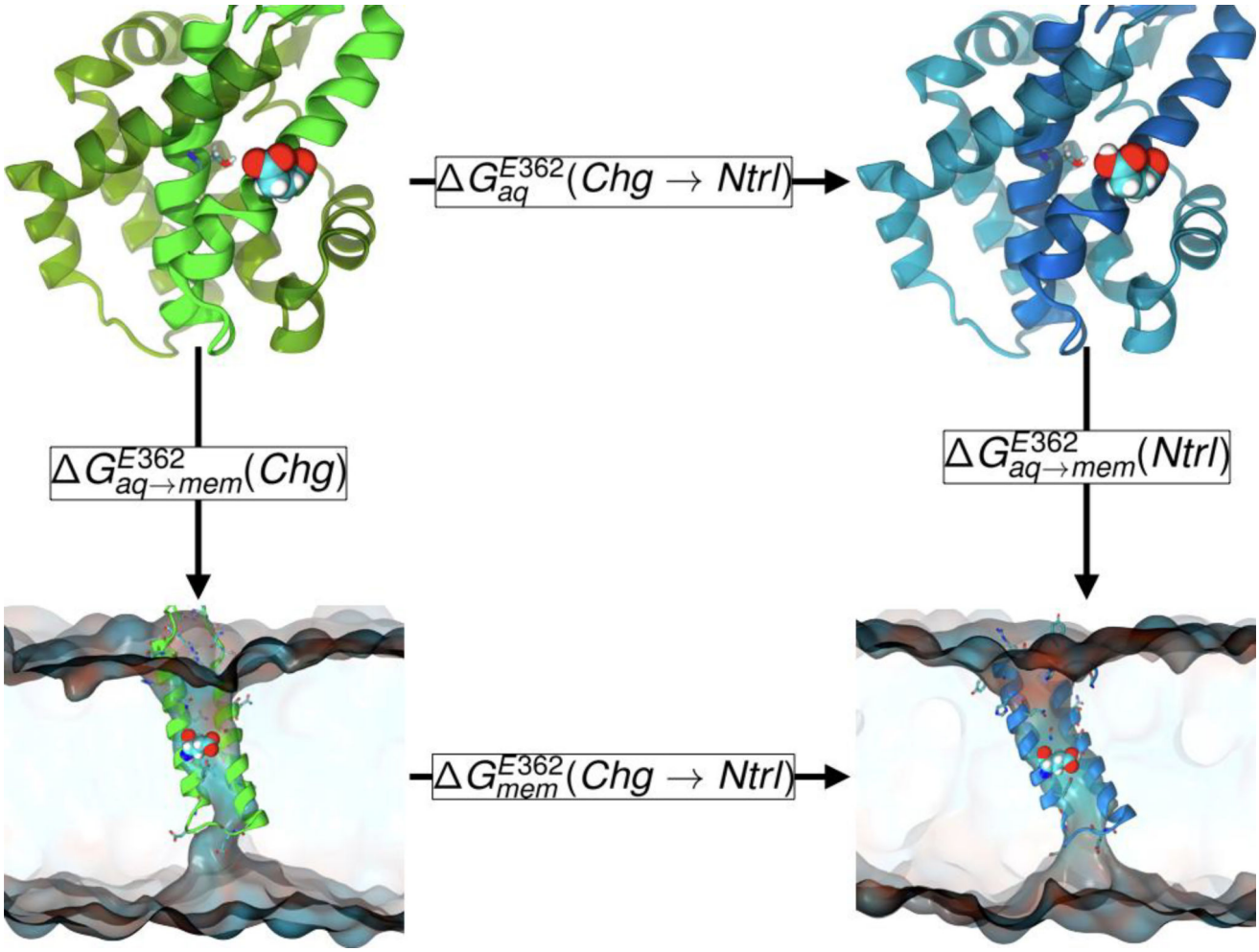

Figure 6.

Thermodynamic cycle for calculating membrane-protein insertion free energies of T-domain for neutralized (Ntrl) E362 relative to charged (Chg) E362. The vertical legs pertain to the membrane insertion free energies of the T-domain, which is obtained from the equivalent horizontal legs calculated from the alchemical free energy calculations. Residue E362 is represented with van der Waals spheres in each image. In the top two images of the protein in solution, the TH8-TH9 helices are shaded differently from the rest of the protein and S336 is displayed to illustrate its position on the TH8 helix relative to E362.

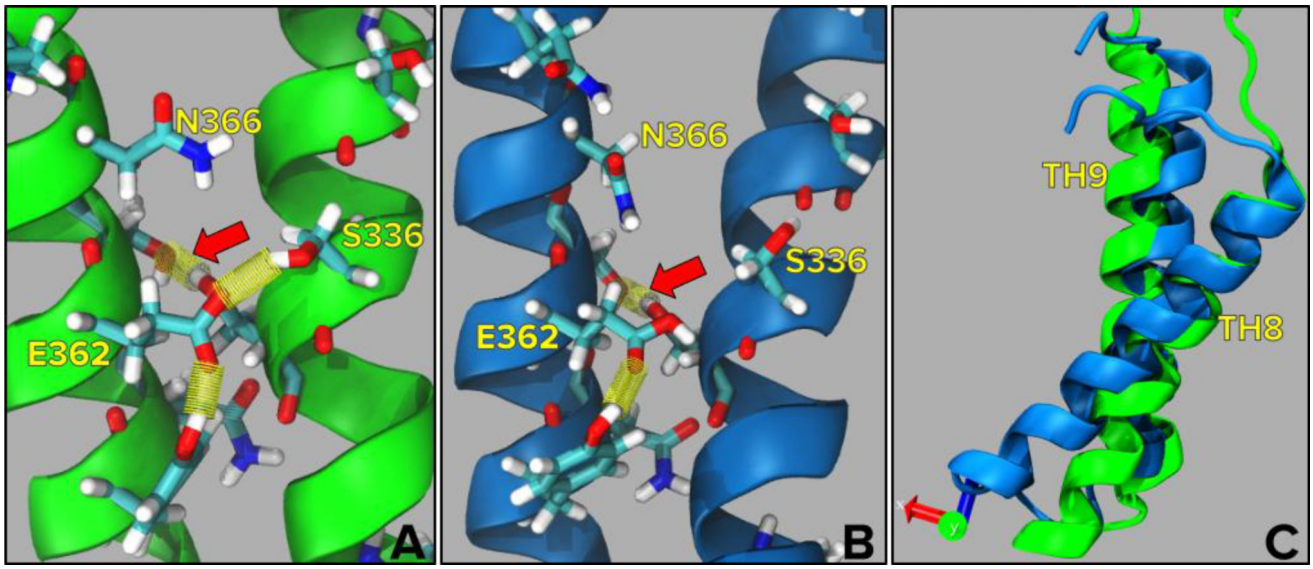

Figure 7.

Hydrogen bond network between the TH8-TH9 helices involving residues S336, S337, E362, S363, and N366. The red arrow points to the H-bond formed between residues S337/S363 which are the two closest points of contacts between the helices. When E362 is charged (Panel A; green), residues N366/S336 are oriented inward but are flipped away when E362 is neutral (Panel B; blue). Panel C shows the shift of the TH8 helix when E362 is charged (green) by overlaying the protein structure from neutralized E362 (blue).

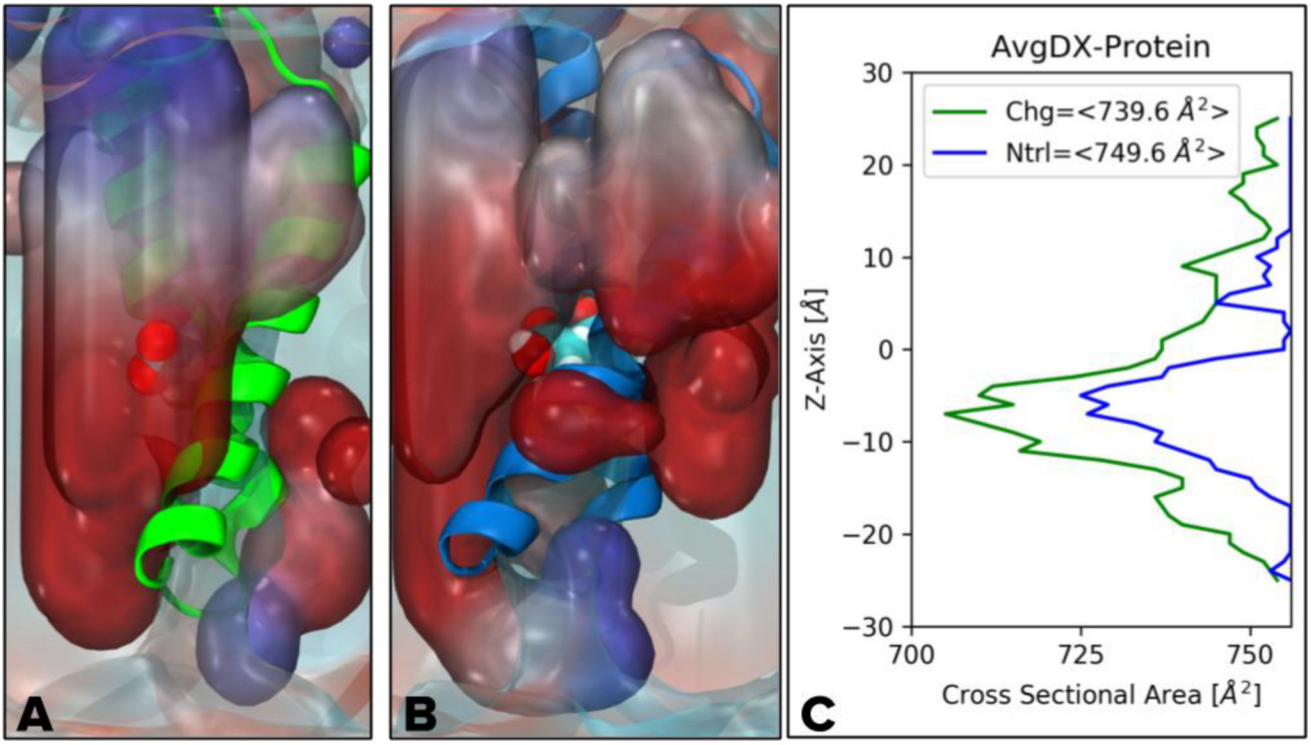

Figure 8.

Solvent accessibility map using average protein and average solvent densities over the 64ns MD simulation. The time-averaged solvent densities are shown for when E362 is charged (Panel A; green) and when E362 is neutral (Panel B; blue). Solvent densities are colored red for high density and blue for low density. Panel C plots the cross-sectional area along the Z-axis with the mean cross-sectional areas being 750 $Å^2$ for neutral E362 and 740 $Å^2$ for charged E362 (Table 3).

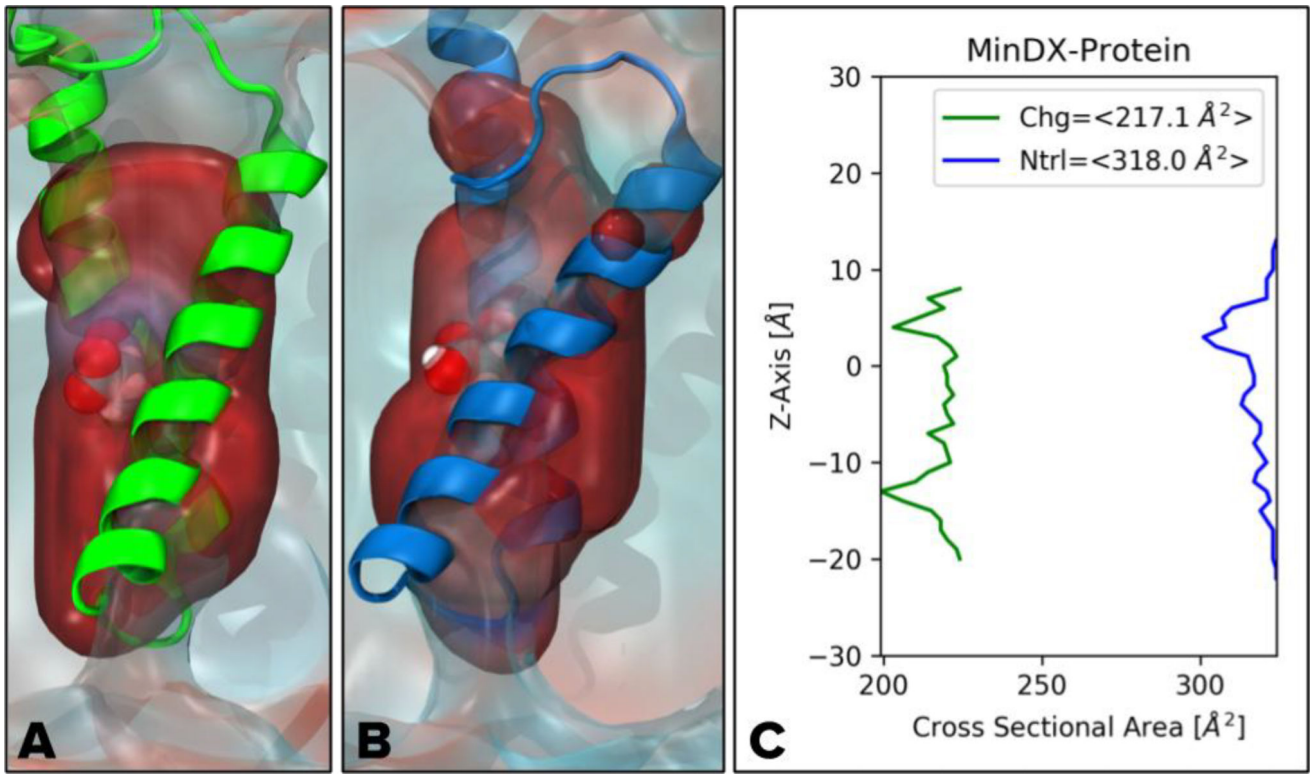

Figure 9.

Maximum solvent accessibility map for when E362 is charged (Panel A; green) and neutral (Panel B; blue), using minimum protein and average solvent densities over the 64ns MD simulation. Panel C plots the cross-sectional area along the Z-axis with the mean cross-sectional areas being 318 $Å^2$ for neutral E362 and 217 $Å^2$ for charged E362 (Table 3).

Table 1

DA parameters estimated from fitting “Differential” Quenching Profiles (i.e., bottom graphs in each panel of Figs. 2, 3, S1, S2): most probable depth of the probe measured from bilayer center, h_m; dispersion of the transverse profile, σ, overall quenching efficiency, *S*.

Samples	h_m(Å)	σ(Å)	*S* (a.u.)
TH-5			
A279C-NBD	0.0±4.2	7.4±0.7	0.82
A282C-NBD	3.2±0.6	6.6±0.7	0.92
TH-6/7			
S305C-NBD	13.5±0.6	3.0±0.5	0.77
S312C-NBD	14.2±0.4	2.9±0.4	0.85
TH-9			
L350C-NBD	14.7±1.0	6.9±1.1	0.21
A356C-NBD	6.5±0.8	6.7±0.7	1.28
N359C-NBD	8.2±1.1	6.6±0.9	0.58
I364C-NBD	3.0±1.7	6.9±2.2	1.42
N366C-NBD	6.9±0.6	6.2±1.6	1.52
Q369C-NBD	10.6±2.1	5.5±1.0	0.65
N373C-NBD	12.1±1.3	6.2±1.2	0.52
P378C-NBD	14.2±0.7	6.2±0.8	0.80

Table 2

Initial and corrected (Shirts and Chodera 2008) free energies obtained from alchemical FEP, transforming E362 from charged to neutral, in the aqueous and membrane environments. The membrane-protein insertion free energies are obtained from the difference in free energies between the two environments.

	$\Delta G \frac{kcal}{mol}$	$\Delta G \frac{kcal}{mol} Corrected$
$\Delta G_{mem}^{E362}(Chg \rightarrow Ntrl)$	84.4	93.3±0.3
$\Delta G_{aq}^{E362}(Chg \rightarrow Ntrl)$	86.0	99.5±0.2
$\Delta\Delta G_{aq \rightarrow mem}^{E362}(Ntrl))$	−1.6	**−6.2±0.4**

Table 3

Mean cross-sectional area along the Z-axis of the pore formed by T-domain when E362 is charged versus neutral. Calculated from dxTuber, using average solvent densities with average versus minimum protein densities.

E362 State	Avg (Å^2)	Min (Å^2)
Neutral	740	318
Charged	750	217